SCIENCE CHINA
Chemistry

•ARTICLES•
SPECIAL ISSUE: 2022 Emerging Investigator Issue

November 2022 Vol.65 No.11: 2188–2196
https://doi.org/10.1007/s11426-022-1315-x

Multi-twinned gold nanoparticles with tensile surface steps for efficient electrocatalytic CO_2 reduction

Li-Wei Chen[1], Yu-Chen Hao[1], Jiani Li[1], Linyu Hu[1], Yu Guo[2], Shuai Li[1], Di Liu[1], Zhejiaji Zhu[1], Si-Qian Wu[1], Hui-Zi Huang[1], An-Xiang Yin[1*], Bo Wang[1] & Ya-Wen Zhang[2]

[1]*Ministry of Education Key Laboratory of Cluster Science, Beijing Key Laboratory of Photoelectronic/Electrophotonic Conversion Materials, Advanced Technology Research Institute (Jinan), School of Chemistry and Chemical Engineering, Beijing Institute of Technology, Beijing 100081, China;*

[2]*Beijing National Laboratory for Molecular Sciences, State Key Laboratory of Rare Earth Materials Chemistry and Applications, PKU-HKU Joint Laboratory in Rare Earth Materials and Bioinorganic Chemistry, College of Chemistry and Molecular Engineering, Peking University, Beijing 100871, China*

Received May 13, 2022; accepted June 22, 2022; published online October 8, 2022

CO_2 reduction reactions (CO_2RR) powered by renewable electricity can directly convert CO_2 to hydrocarbons and fix the intermittent sustainable energy in portable chemical fuels. It is of great importance to develop advanced catalysts that can boost CO_2RR with high activity, selectivity, and efficiency at low overpotentials. Here, we report the solution synthesis using H_2O_2 to modify the surface structures of gold multi-twinned nanoparticles (AuMPs) and create tensile surface steps. Calculations predicted significantly enhanced CO_2 adsorption and boosted CO_2RR capabilities with inhibited hydrogen evolution reaction activity for the tensile surface steps with modified electronic structure. The H_2O_2-treated AuMPs with surface steps and 3.83% tensile lattices showed much higher activity and selectivity at lower overpotentials for CO_2RR than pristine gold nanoparticles. The CO-production current density reached about 98 mA cm^{-2} with a Faradaic efficiency of 95.7% at –0.30 V versus reversible hydrogen electrode in the flow cell, showing a half-cell energy efficiency as high as ~83%. Our strategy represents a rational catalyst design by engineering the surface structures of metal nanoparticles and may find more applicability in future electrocatalysis.

gold nanoparticles, tensile lattice, surface steps, electrocatalysis, CO_2 reduction

Citation: Chen LW, Hao YC, Li J, Hu L, Guo Y, Li S, Liu D, Zhu Z, Wu SQ, Huang HZ, Yin AX, Wang B, Zhang YW. Multi-twinned gold nanoparticles with tensile surface steps for efficient electrocatalytic CO_2 reduction. *Sci China Chem*, 2022, 65: 2188–2196, https://doi.org/10.1007/s11426-022-1315-x

1 Introduction

Electrochemical reduction of carbon dioxide (CO_2) to carbon monoxide (CO) represents a crucial route for the renewable C_1 transformation [1–3]. Efficient CO_2 reduction reaction (CO_2RR) requires higher activity and selectivity at lower overpotentials, which, however, has been limited by the considerable kinetic barriers for CO_2 activation and the intense hydrogen evolution reaction (HER) competitions [4–7]. Gold (Au) electrocatalysts have been studied intensively nowadays for promoting the CO_2-to-CO conversion [8–23].

To date, two major strategies have been developed to modulate Au-based electrocatalysts. The first one is to modify their surface geometric structures, such as morphologies [14,16], sizes [13], grain boundaries [15,18], and surface defects [8,20]. The second one is to tailor their surface electronic structures by decorating Au nanoparticles (AuNPs) with other molecules [17,22] or substrates [23].

*Corresponding author (email: yin@bit.edu.cn)

Such results suggest that the CO_2RR reactivity of Au-catalysts could be generally promoted by creating more surface-active sites with higher intrinsic activities by modifying their geometric and electronic structures. However, comprehensive and thorough studies on the fundamental principles for CO_2RR on Au surfaces remain elusive. Practical Au-catalyzed CO_2RR applications with high energy efficiency still require the systematic optimization of both the catalytic centers and the reaction interfaces.

Here, we report the synthesis of free-standing Au multi-twinned nanoparticles (AuMPs) with tunable surface dislocations and tensile lattices through a solution approach involving hydrogen peroxide (H_2O_2) as a structure modifying agent. Transmission electron microscopy (TEM) characterizations, spectroscopic measurements, and computational studies revealed that the H_2O_2-modified AuMPs (denoted as H-AuMPs) exhibited high-density surface dislocations and tensile lattices (Figure 1a). The modified surface geometric and electronic structure thereby selectively strengthened the adsorption of CO_2 species and boosted the rate-determining step (RDS) of CO_2RR on Au surfaces. As a result, the H-AuMPs with the lattice tension of 3.83% showed a CO partial current density (j_{CO}) of 10 mA cm^{-2} at just –0.175 V versus reversible hydrogen electrode (*vs*. RHE) in the membrane flow cell (Figure 1b), exhibiting an overpotential as low as 65 mV for CO_2RR. Even higher and stable j_{CO} (~98 mA cm^{-2}) and Faradaic efficiency (FE, ~96%) can be achieved at –0.30 V *vs*. RHE, with a half-cell energy efficiency as high as ~83% in long-term (> 40 h) CO_2RR tests.

2 Experimental

2.1 Materials

Gold(III) chloride trihydrate ($HAuCl_4{\cdot}3H_2O$, ≥49.0% Au basis), sodium borohydride ($NaBH_4$, 99%), deuteroxide (D_2O), and Nafion (5% in methanol) were purchased from Sigma-Aldrich (USA). Ethylene glycol (99%), potassium bicarbonate ($KHCO_3$, >99.9%), and carbon black (acetylene black, 50% compressed, >99.9%) were purchased from Alfa Aesar (USA). Oleylamine (OAm, $C_{18}H_{37}N$, C_{18}: 80%–90%) was purchased from Energy Chemical (China). Hydrogen peroxide (H_2O_2, 30 wt%) was purchased from Tianjin Fengchuan Chemical Reagent Co. Ltd. (China). Cyclohexane (C_6H_{12}) and absolute ethanol (C_2H_5OH, 99.5%) were purchased from Beijing Tong Guang Fine Chemicals Company (China). All chemicals were used as received without further treatment. All glassware was cleaned using aqua regia, followed by rinsing with copious amounts of ultrapure water. Ultrapure water (18.2 MΩ cm at 25 °C) obtained by a Milli-Q system was used in all experiments.

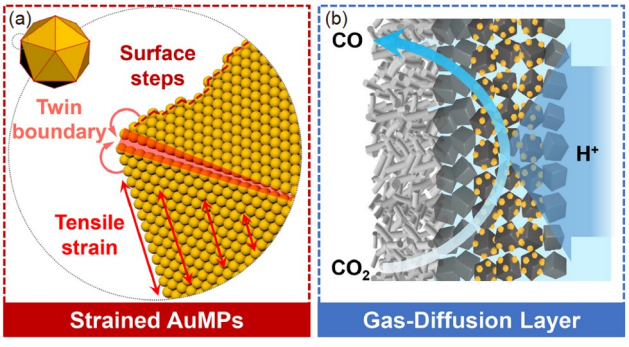

Figure 1 Schematic illustration for the strategy of promoting CO_2 reduction with optimized catalysts and reaction interface. (a) The existence of twin boundaries, surface steps, and tensile strain modifies the surface geometric and electronic structures of Au catalysts for promoted CO_2 reduction. (b) Schematic for the reaction interface modification. The Au catalysts were loaded on the gas-diffusion layer that can facilitate the diffusion of CO_2 gas to the catalyst surface (color online).

2.2 Synthesis of H-AuMPs

Typically, 4 mg of $HAuCl_4{\cdot}3H_2O$ was added into a 25 mL round bottom flask containing 9.5 mL of OAm. The mixture was sonicated at room temperature until the chloroauric acid was completely dissolved. Then, the mixture solution of 0.30 mL of H_2O_2 and 0.20 mL of H_2O was dropwise added into the flask. The mixture was sonicated until the precipitate was fully dissolved and then stirred and refluxed at 120 °C for 30 min. The solution gradually turned from pale yellow to cloudy, became colorless after about 5 min, and finally became deep red.

2.3 Synthesis of P-AuMPs

Typically, 4 mg of $HAuCl_4{\cdot}3H_2O$ was dissolved in 10 mL of OAm under sonication. The solution was stirred and heated at 120 °C for 30 min. The solution turned from pale yellow to colorless and then dark red.

2.4 Collecting and washing of AuMPs

After reacting for 30 min, 30 mL of absolute ethanol was poured into the reaction solution to quench the reaction. The products were separated by centrifugation (8,000 r mim^{-1}, 10 min). The precipitates were washed (with cyclohexane and ethanol) and centrifuged (8,000 r min^{-1}, 10 min), and then redispersed in cyclohexane.

2.5 Loading AuMPs on carbon black (CB) supports

Typically, 18 mg of CB was added to 4 mL of cyclohexane and ultrasonicated for 40 min. Afterwards, the as-prepared AuMPs (dispersed in cyclohexane) were added dropwise under vigorous stirring. The solution was sonicated for 40 min and centrifuged at 9,000 r mim^{-1} for 8 min. The

precipitates were collected and dried at 40 °C in a vacuum oven. The as-obtained H-AuMPs/CB and P-AuMPs/CB catalysts were heated at 200 °C in air with a tube furnace for 1.5 h to remove the organic residuals adsorbed on the Au surfaces.

2.6 Synthesis of AuNPs/CB catalysts

Typically, 18 mg of CB was fully dispersed in 10 mL of anhydrous ethylene glycol and sonicated for 3 h, followed by the addition of 400 μL of 25.4 mM $HAuCl_4$ ethylene glycol solution. The mixture solution was then vigorously stirred at room temperature for 40 min and sonicated for another 3 min. After that, 1.2 mL of 0.1 M freshly prepared, ice-cold $NaBH_4$ ethanol solution was injected into the mixture solution dropwise under vigorous stirring (1,200 r mim^{-1}). After another 30 min of continuous stirring, the final product was collected by centrifuge, washed with ethanol three times, and finally dried at 40 °C under vacuum. The as-prepared powder was annealed at an elevated temperature of 500 °C for 1 h in a tube furnace in air with a heating rate of 5 °C min^{-1}.

2.7 Characterizations

Powder X-ray diffraction (PXRD) was performed on a Rigaku MiniFlex 600 diffractometer with a Cu-Kα X-ray radiation source (λ = 0.154056 nm) at the scan rate of 1° min^{-1}. X-ray photoelectron spectroscopy (XPS) measurement was obtained by a Thermo VG ESCALAB-250 system with Al-Kα and Mg-Kα sources operated at 15 kV. The binding energies were referred to the C 1s peak (284.8 eV) from adventitious carbon. Inductively coupled plasma-optical emission spectrometry (ICP-OES) was measured on an Agilent ICP-OES 720 spectrometer. The Au L-edge XAFS spectra were obtained at beamline BL01C1 of the "National" Synchrotron Radiation Research Center (NSRRC, Taiwan, China). The samples were measured in the fluorescence mode by using a solid detector to collect the data. Gold foil was used as standard reference material for these measurements. Athena and Artemis codes were used to extract the data and fit the profiles. For the X-ray absorption near-edge structure (XANES) part, the experimental absorption coefficients as a function of energies $\mu(E)$ were processed by background subtraction and normalization procedures and reported as normalized absorption for all the measured samples and standard references. Transmission electron microscopy (TEM) studies were performed on a JEM-2100 (JEOL) microscope operated at 200 kV, and a Tecnai G2 F30 (FEI) microscope worked at 300 kV. For atomic resolution imaging, the measurements were performed on an FEI Titan Themis at 200 kV with spherical aberration corrected under high-angle annular dark-field scanning TEM (HAADF-STEM) mode.

2.8 Electrolysis tests in H-type cell

General electrochemical measurements were carried out in a three-electrode system with an H-type electrolysis cell. The cathodic and anodic compartments were separated by a Nafion 115 proton exchange membrane. The membrane was pretreated in 5% H_2O_2 solution (80 °C, 1 h), soaked in 0.5 M H_2SO_4 solution (80 °C, 1 h), immersed in ultrapure water (80 °C, 1 h), and then washed with ultrapure water several times before use. A platinum plate (1 × 1 cm^2) and a saturated calomel electrode (SCE) were used as the counter electrode and the reference electrode, respectively. All potentials were measured against the SCE and converted to the RHE scale according to the Nernst equation.

Catalyst inks were prepared by dispersing 10 mg of Au/CB catalysts in the mixture of 80 μL of Nafion, 0.75 mL of isopropanol, and 0.25 mL of water under sonication (40 min). The working electrode was made by applying about 175 μL of the catalyst ink on the carbon paper (Toray TGP-H-060) with an effective electrode geometric area of 1 × 1 cm^2 and a metal (Au) loading of about 0.16 mg cm^{-2}.

Freshly prepared 0.5 M $KHCO_3$ aqueous solutions were used as electrolytes. The electrolytes were purged with high-purity (99.9999%) argon for at least 40 min and then with high-purity (99.999%) CO_2 for another 40 min before the CO_2RR tests. During electrolysis tests, the cathodic electrolyte was magnetically stirred at 800 r mim^{-1} and bubbled with CO_2 gas at 60 mL mim^{-1}. An online gas chromatograph (GC, Shimadzu GC-2014C) equipped with a packed column (MS-13X), a thermal conductivity detector (TCD), and a flame ionization detector (FID) was used to quantify the gaseous products. And the possible liquid products were analyzed by ^{1}H nuclear magnetic resonance (NMR). A 90% ohmic resistance correction was applied in all the measurements. All tests were conducted at ambient pressure and room temperature unless other noted.

2.9 Electrolysis tests in flow cells

A membrane flow cell composed of a gas-diffusion electrode (GDE) and an anion exchange membrane was used. An SCE was fixed in the cathode chamber as the reference electrode, and a platinum plate was fixed in the anode chamber as the counter electrode. A freshly prepared 0.5 M $KHCO_3$ solution was used as the cathodic electrolyte and was circulated (20 mL mim^{-1}) through the electrochemical cell using a peristaltic pump.

Catalyst inks were prepared by dispersing 10 mg of Au/CB catalysts in the mixture of 80 μL of Nafion, 1.5 mL of isopropanol, and 0.50 mL of water under sonication for 40 min. Additional CB inks were prepared by dispersing 4 mg of CB in the mixture of 100 μL of Nafion, 1.50 mL of isopropanol, and 0.50 mL of water under sonication for 1 h. The GDE was

made by seriatim applying about 1.25 mL of the catalyst ink and 1.05 mL of the CB ink on the carbon-based gas-diffusion layer (GDL) substrate (Freudenberg, Germany) by vacuum filtration with an effective electrode geometric area of 3.14 cm^2 (diameter = 2 cm) and a metal (Au) loading of about 0.19 mg cm^{-2}.

During the CO_2RR tests, high-purity (99.999%) and pre-humidified CO_2 gas was delivered to the cathode with a constant flow rate of 60 mL mim^{-1} monitored by a mass flow controller. Similarly, the gaseous and liquid products were quantified by the online GC and NMR, respectively. A 90% ohmic resistance correction was applied in all the measurements. All tests were conducted at ambient pressure and room temperature unless other noted.

3 Results and discussion

3.1 Electrocatalyst synthesis and characterization

We prepared the H-AuMPs by reducing chloroauric acid ($HAuCl_4$) in a mixture of OAm, H_2O, and H_2O_2. TEM study showed the freestanding and monodispersed H-AuMPs with a size distribution of 9.6±1.9 nm (Figure 2a and Figure S1 (Supporting Information online)). What is more, the obvious fringes showed by TEM and the widened diffraction rings revealed by the selected area electron diffraction patterns (Figure 2b and Figure S2) suggested the highly dislocated surface features of the H-AuMPs [24,25]. In comparison, pristine AuMPs (denoted as P-AuMPs, Figures S2–S4) prepared in sole OAm (without H_2O or H_2O_2), as well as ordinary gold nanoparticles (denoted as AuNPs, Figures S5 and S6) prepared by reducing $HAuCl_4$ with strong reductant sodium borohydride ($NaBH_4$), showed relatively smooth surfaces with fewer surface defects. High-resolution TEM (HRTEM) images suggested the existence of abundant stacking faults intersecting with each other on the surface of H-AuMPs (Figure 2b), which may create dense surface defects [26]. Aberration-corrected high-angle annular dark-filed scanning TEM (AC-HAADF-STEM) images (Figure 2c, d) revealed the surfaces steps on H-AuMPs, which could thereby create catalytically active sites due to their under-coordinated chemical states [2,15,18].

X-ray diffraction (XRD) patterns (Figures S7 and S8) suggested the existence of tensile lattice in the as-obtained H-AuMPs. Compared to the P-AuMPs and AuNPs with standard lattice spacings for Au (PDF#04-0784), the Au (111) and (200) diffraction peaks for H-AuMPs were significantly shifted to lower angles (Figure S7), suggesting the stretched lattices for H-AuMPs [27]. Therefore, in synthesis, with strong redox and etching activity, hydrogen peroxide could perturb the nucleation and growth stage of Au nanocrystals, triggering the formation of high-density stacking

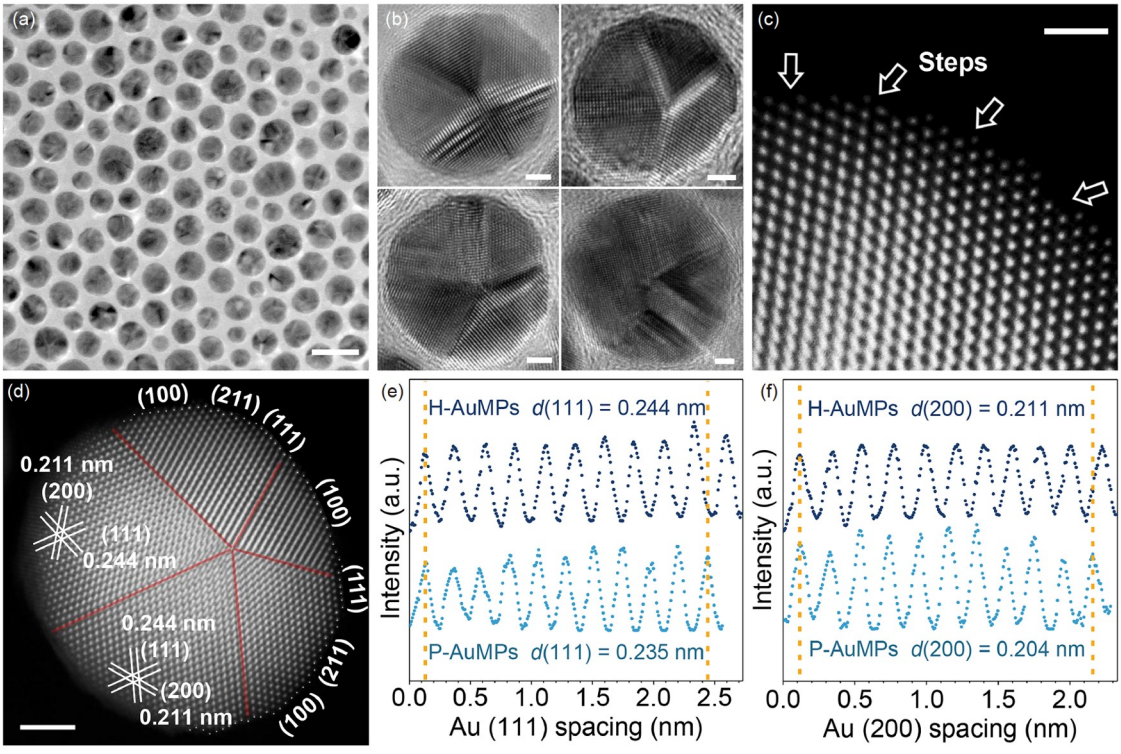

Figure 2 Morphology and structure characterization of H-AuMPs. (a) TEM image, (b) HRTEM images, and (c, d) AC-HAADF-STEM images for the as-prepared H-AuMPs. The arrows in (c) denote the surface atomic steps. The red lines in (d) indicate the grain boundaries of H-AuMP. (e, f) Integrated pixel intensities of H-AuMPs and P-AuMPs for 10 periods along the Au (111) and (200) directions, respectively. Scale bars: (a) 20 nm, (b) 2 nm, (c) 1 nm, and (d) 2 nm (color online).

faults (Figures S9, S10) [28]. Such abundant stacking faults thereby endowed the H-AuMPs with more lattice distortions and surface defects compared with the P-AuMPs [29].

The XRD patterns reflected the averaged lattice parameters and suggested the general trend of lattice stretching for H-AuMPs. More detailed information was provided by the AC-HAADF-STEM images showing the precise surface structures of nanoparticles [29,30]. As shown in Figure 2d, the H-AuMP was enclosed by the basal (111), (100) planes and the stepped (211) facets. Moreover, measurements of the (111) and (200) lattice spacings revealed significant differences between the H-AuMPs and the P-AuMPs/AuNPs (Figure 2e, f and Figures S11–S13). The (111) and (200) lattice spacings for P-AuMPs and AuNPs were about 0.235 and 0.204 nm, respectively, both of which were well consistent with the standard lattice spacings for Au (PDF#04-0784). By sharp contrast, the H-AuMPs exhibited the averaged spacings of 0.244 and 0.211 nm for Au (111) and (200) planes, respectively, indicating the existence of ~3.83% tensile change on the surfaces of H-AuMPs. In short, we have prepared three typical Au nanocatalysts, among which the twinned H-AuMPs possessed high-density surface steps and tensile lattices, the twinned P-AuMPs showed mostly smooth surfaces and normal lattices, and the single-crystalline AuNPs exhibited smooth surfaces and pristine lattices.

3.2 Mechanism investigation

The surface electronic structures of the Au nanocrystals would be significantly altered by incorporating tensile lattices. As expected, X-ray absorption near-edge structure spectroscopy (XANES) and X-ray photoemission spectroscopy (XPS) studies suggested that all three samples (*i.e.*, H-AuMPs, P-AuMPs, and AuNPs) comprised the same pure Au^0 phase (Figures S14 and S15). However, the valence band (*i.e.*, 5d band) of the H-AuMPs was clearly shifted upward compared with that of P-AuMPs, AuNPs, and the standard reference, according to the surface valence band spectra (Figure 3a) and the density functional theory (DFT) calculations (Figure 3b). The tensile change of 3.83% could shift the 5d band centers of the Au (111) and (211) planes upward by 0.09 and 0.12 eV, respectively. According to the fundamental principles of surface chemistry and coordination chemistry [31], the upward shift of the outermost d-bands of transition metals would thereby push more portion of the anti-bonding states for the metal-adsorbate bonds above the Fermi level. As a result, the anti-bonding states would be less occupied, and the adsorption between the metal surface and

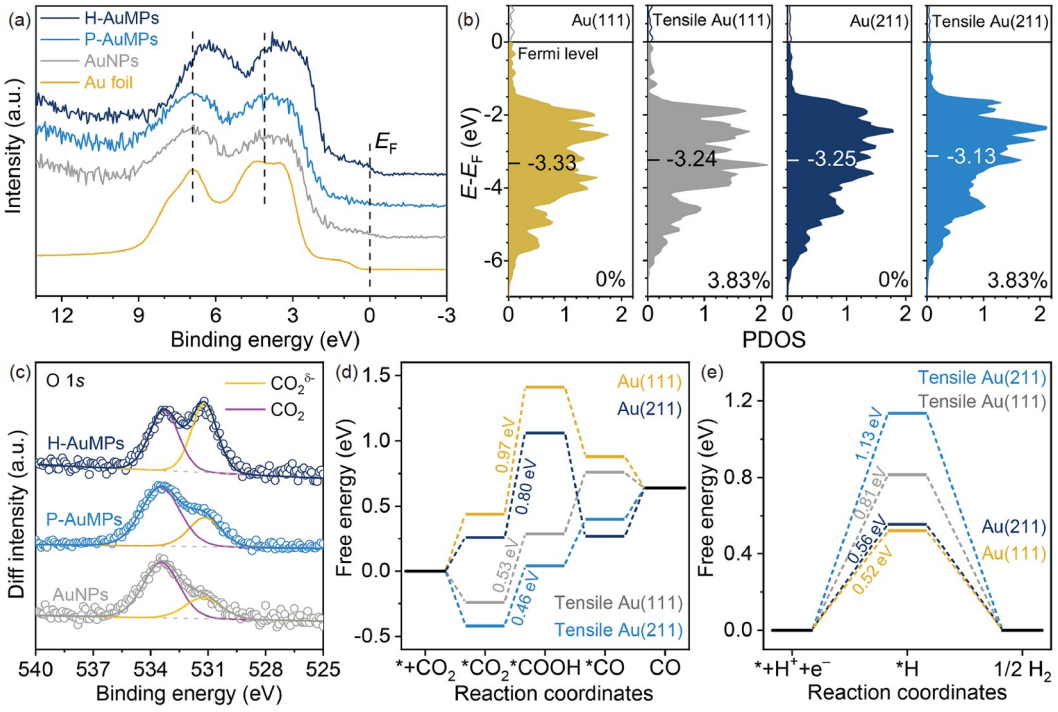

Figure 3 X-ray photoelectron spectra and density functional theory calculations for the surface electronic structures, CO_2 adsorption, and reaction coordinates on different Au particles. (a) Surface valence band photoelectron spectra of H-AuMPs, P-AuMPs, AuNPs, and the standard Au foil reference. All the spectra are background corrected. The d-band and its center of gravity for H-AuMPs exhibited obvious migration to the Fermi level (E_F) compared with that for P-AuMPs, AuNPs, and the standard Au foil reference. (b) DFT-calculated projected density of states (PDOS) for Au 5d bands of Au (111) and Au (211) surfaces with the tensile strain of 0 (corresponding to P-AuMPs and AuNPs) and 3.83% (corresponding to H-AuMPs), respectively. The centers of the d-bands were also labeled. (c) The intensity changes in O 1s core-level XPS spectra induced by CO_2 adsorption on three catalysts. (d, e) Schematic energetics of elementary reaction steps for CO_2RR (d) and HER (e) at 0 V*vs*. RHE on flat Au (111) facet and stepped Au (211) facet with/without 3.83% tensile lattice (color online).

the adsorbates would be thereby strengthened [32]. In the case of CO_2RR, the surface atoms of H-AuMPs would then bond with the adsorbates (*e.g.*, *CO_2) much more strongly than that of P-AuMPs and AuNPs due to their upshifted 5d bands [33,34]. Enhancing CO_2 adsorption on Au surfaces would theoretically promote CO_2RR since Au showed relatively weak adsorption to CO_2 species and was located on the right side of the volcano plot for CO_2RR [35,36].

The theoretically predicted strengthened CO_2 adsorption on H-AuMPs was supported by the CO_2-adsorption-induced differential XPS spectra. As shown in Figure 3c, the O 1s core-level XPS spectra could be de-convoluted into two oxygen species, the physically adsorbed CO_2 (533.4 eV) and the chemically adsorbed $CO_2^{\delta-}$ species (531.2 eV) [37]. The portions for $CO_2^{\delta-}$ species were much higher on H-AuMPs than that on the other two samples. That is, with abundant surface defects and tensile lattices, H-AuMPs exhibited much stronger chemical bonding with CO_2 than P-AuMPs and AuNPs.

We employed DFT calculations to predict further the adsorption and electrocatalytic conversion of CO_2 on Au surfaces [38–44]. According to the TEM analysis, the flat surface of obtained three Au catalysts mainly exposed the (111) facet (Figures S11–S13), while the stepped surface of H-AuMPs predominantly exposed the (211) facet (Figure 2d). Therefore, the structure-sensitivity of CO_2RR was studied on both flat (111) and stepped (211) Au surfaces with/without 3.83% tensile lattices. We calculated the most stable adsorption structures and energetics of *CO_2, *COOH, and *CO for CO_2RR (and *H for the competing HER) on the Au (111) and (211) facets with and without tensile lattice (see Calculation Methods and Figures S16, S17 for details on the construction of these models and the respective optimized lattice constants). The free energy diagrams of CO_2RR and HER on these model surfaces are reported in Figure 3d and 3e, respectively (Tables S1–S6 list the calculated Gibbs free energy and relevant parameter).

Generally, the electrocatalytic reduction of CO_2 to CO on Au surfaces in aqueous solutions would comply with the following steps [13,35,36]:

$$* + CO_2 \rightarrow *CO_2 \quad (1)$$

$$*CO_2 + H^+ (aq) + e^- \rightarrow *COOH \quad (2)$$

$$*COOH + H^+ (aq) + e^- \rightarrow *CO + H_2O \quad (3)$$

$$*CO \rightarrow * + CO \quad (4)$$

where the asterisk (*) denoted a catalytically active site at the surface. According to previous reports, the CO_2 adsorption strength could be used as a descriptor for CO_2RR on Au surfaces as Au was located on the right side of the CO_2RR volcano plot and exhibited weaker adsorption of CO_2 species [9,35,36]. Notably, the tensile Au surface exhibited significantly promoted CO_2 adsorption with both experimental (Figure 3c) and theoretical (Figure 3d) evidence. Moreover, the potential-determining step (PDS) was the first one-electron transfer path (Figure 3d). The tensile facets could lower the free energy requirement for the PDS and thus enhance the CO_2RR reactivity. Especially, the tensile stepped Au (211) facet, showing the lowest PDS energy barrier of 0.46 eV (at 0 V *vs*. RHE), would hold the possibility to boost the CO_2 reduction process significantly (Figure 3d). On the other hand, for the proton involved CO_2RR, an efficient catalyst needed not only to promote the adsorption and activation of CO_2 but also to inhibit the direct reduction of H^+ to H_2 (*i.e.*, HER). As shown in Figure 3e, the tensile effect could obviously increase the energy barrier for HER on both the flat Au (111) facet and the stepped Au (211) facet, indicating that HER should be effectively inhibited on the H-AuMPs. Similar inhibition of HER by tensile strain could be found in Pd and Cu catalysts [32,45–47], showing that strain engineering could benefit CO_2RR electrocatalysis indirectly by suppressing the competing HER.

3.3 CO_2RR performance in H-type cell

The CO_2RR performances for different catalysts (*i.e.*, H-AuMPs, P-AuMPs, and AuNPs) were first tested in a two-component, three-electrode electrochemical cell with 0.5 M potassium bicarbonate (saturated by high-purity CO_2) as electrolyte. XPS survey revealed that no nitrogen residuals on the surface of AuMPs could be detected, suggesting the removal of possible OAm species on the catalyst surface (Figure S18). The working electrode was prepared by applying catalysts on hydrophobic carbon paper (CP, the effective geometric area was fixed at 1 cm^2) with a metal loading of about 0.16 mg cm^{-2}. The cathodic electrolyte was magnetically stirred at 800 r min^{-1} and bubbled with high-purity CO_2 gas at the flow rate of 60 sccm (standard cubic centimeter per minute) during electrolysis tests. The gas products were measured by online gas chromatography (GC), and the liquid products were analyzed by ^{1}H nucleic magnetic resonance (NMR). The linear sweep voltammetry results of CO_2RR on AuNPs, P-AuMPs, and H-AuMPs (Figure 4a) revealed that the onset of CO_2 reduction on H-AuMPs required a much smaller overpotential than that on the other two samples. CO production could be detected on H-AuMPs with an FE of ~8% and a j_{CO} of ~0.3 mA cm^{-2} when the cathodic potential was set at –0.15 V *vs*. RHE, with the corresponding overpotential of only 40 mV (Figure 4b, c). In sharp contrast, detectable CO_2RR on P-AuMPs and AuNPs was observed at the cathodic potential of –0.30 V *vs*. RHE, with the overpotential of 190 mV (Figure 4b and Figures S19, S20). Moreover, H-AuMPs exhibited the highest FE and j_{CO} values among the three catalysts at all tested cathodic potentials (–0.15 to –0.6 V *vs*. RHE). The FE value for CO production on H-AuMPs catalyst was increased rapidly as the cathodic potential decreased from –0.15 to –0.25 V *vs*. RHE and then maintained above 90% in a wide

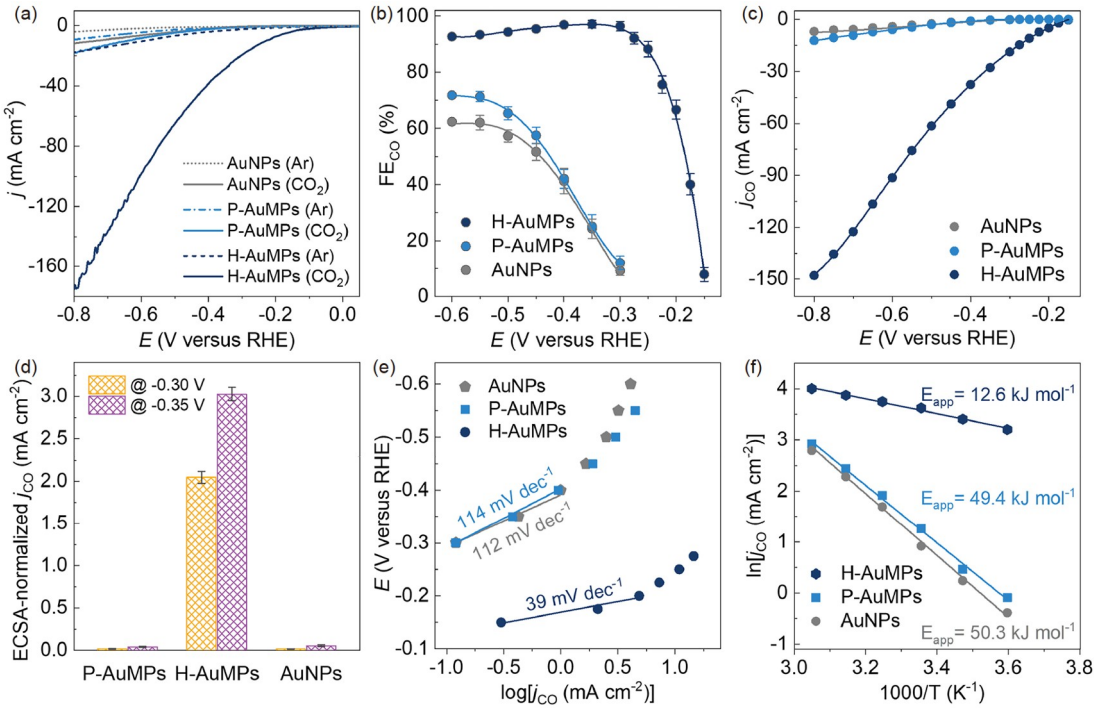

Figure 4 CO_2 electroreduction on Au catalysts tested in an H-type cell. (a) Linear sweep voltammetry (LSV) curves for electrocatalytic reactions on AuNPs, P-AuMPs, and H-AuMPs in Ar- and CO_2-saturated 0.5 M potassium bicarbonate ($KHCO_3$) solution. (b) Faradaic efficiencies and (c) CO partial current densities *vs*. the potential over different samples in an H-type cell. (d) The ECSA-normalized CO partial current densities at –0.30 and –0.35 V*vs*. RHE on three catalysts. (e) Tafel plots for the conversion of CO_2 to CO on three catalysts. (f) Apparent activation energies (E_{app}) for CO_2RR on different catalysts (at –0.5 V*vs*. RHE). The E_{app} values were derived from the slope of their Arrhenius plots (color online).

potential window. At –0.3 V *vs*. RHE, H-AuMPs exhibited the maximum FE of 96.4% with a j_{CO} of ~19 mA cm^{-2}. In contrast, P-AuMPs and AuNPs showed the FE of ~12% and ~9%, and the j_{CO} of ~0.16 and ~0.12 mA cm^{-2} at –0.3 V *vs*. RHE, respectively (Figure 4b, c). In addition, given the similar electrochemical active surface area (ECSA) (Figure S21), the H-AuMPs exhibited an ECSA-normalized j_{CO} (2.05 mA cm^{-2}) at –0.3 V *vs*. RHE, which was more than 100 times higher than that on P-AuMPs (0.018 mA cm^{-2}) and AuNPs (0.016 mA cm^{-2}) (Figure 4d). These results clearly suggested that the highly dislocated Au surfaces with high-density steps and strong tensile lattice can boost CO_2RR efficiently. The Tafel slopes for CO formation on H-AuMPs, P-AuMPs, and AuNPs were 39, 114, and 112 mV dec^{-1}, respectively (Figure 4e). The Tafel slope of 114 and 112 mV dec^{-1} measured on the P-AuMPs and AuNPs agreed well with prior reports [12,20], suggesting that the first one-electron transfer step would be the RDS for the reaction [12,16,20,22]. However, the much lower Tafel slope of 39 mV dec^{-1} obtained for the H-AuMPs indicated a much faster first-electron transfer step [12,16] and therefore boosted CO_2RR on H-AuMPs. Additional evidence could be found in the apparent activation energy (E_{app}) for CO_2RR on the three catalysts at –0.5 V *vs*. RHE (Figure 4f). P-AuMPs and AuNPs exhibited similar E_{app} for CO_2RR (49.4 and 50.3 kJ mol^{-1}, respectively). In contrast, H-AuMPs showed a much lower E_{app} of about 12.6 kJ mol^{-1}, further highlighting that the rich surface steps and tensile lattice could alter the RDS and decrease the overall kinetic barriers for CO_2RR on Au surfaces. Therefore, proved by both calculation and experiments, creating surface steps and tensile lattices on Au catalysts can modify the electronic structures of the catalytic sites, strengthen the adsorption of CO_2 species, lower the reaction energy barrier, and promote CO_2RR efficiently.

3.4 CO_2RR performance in a gas flow cell

As reported [48–50], the CO productivity of CO_2RR would be (partially) limited by the sluggish CO_2 diffusion in aqueous solutions. To boost the CO_2-to-CO conversion further, we then applied the H-AuMPs to the GDE with a mass loading of 0.19 mg cm^{-2} and measured CO_2RR in a flow cell (Figure S22). The GDE was made by seriatim applying the catalyst ink and another carbon black (CB) ink on the carbon-based gas-diffusion layer (GDL) substrate by vacuum filtration. The additional layer of CB would help maintain the hydrophobicity of the reaction interface to avoid GDL flooding during CO_2RR tests [48]. In typical CO_2RR tests, high-purity (99.999%) pre-humidified CO_2 gas was delivered to the cathode with a constant flow rate of 60 sccm.

The GDE-supported H-AuMPs exhibited a significantly boosted and stable total current density of ~105 mA cm^{-2} with the FE_{CO} of ~95% at –0.3 V *vs*. RHE during the long-term (> 40 h) stability test (Figure 5a). The j_{CO}

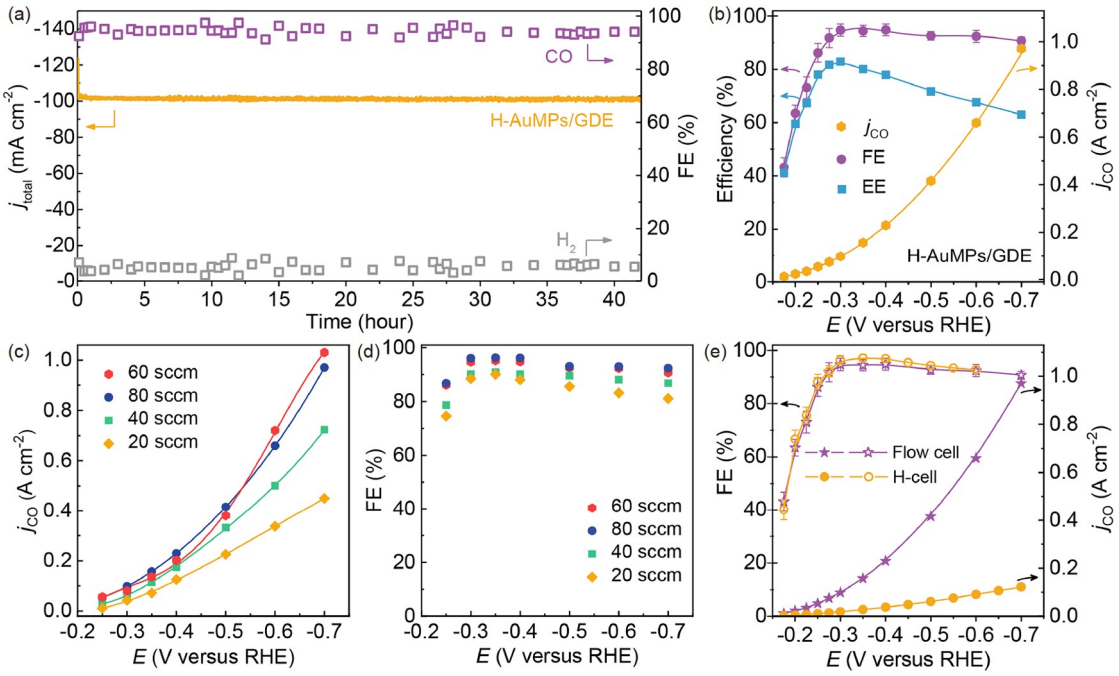

Figure 5 CO_2 electroreduction on GDE-supported H-AuMPs in a flow cell. (a) Total chronoamperometry curve (left axis) and Faradaic efficiency for CO and H_2 production (right axis) *vs*. time on H-AuMPs in the flow cell at the cathodic potential of –0.3 V*vs*. RHE. (b) FE of CO and half-cell energy efficiency (EE, left axis) and CO partial current density for CO_2RR on H-AuMPs at various cathodic potentials (with iR correction) in the flow cell. The flow rate for humidified CO_2 was fixed at 60 sccm for panels (a, b). (c) CO partial current density and (d) corresponding Faradaic efficiency on H-AuMPs catalysts at various cathodic potentials in the flow cell with different CO_2 flow rates. (e) Faradaic efficiency (left axis) and corresponding CO partial current density (right axis) on H-AuMPs catalysts in the H-cell and flow cell, respectively (color online).

(~98 mA cm^{-2}) exceeded 5 times that (~19 mA cm^{-2}) obtained in the conventional H-cell at –0.3 V *vs*. RHE. The FE_{CO} on GDE-supported H-AuMPs was increased rapidly as the cathodic potential decreased from –0.15 to –0.25 V *vs*. RHE and then held above 90% in a wide potential window from –0.275 V to –0.7 V *vs*. RHE. Notably, at –0.3 V *vs*. RHE, the H-AuMPs exhibited a maximum half-cell energy efficiency (EE) as high as ~83% with an FE of 94.7% and a j_{CO} of 98.4 mA cm^{-2} (Figure 5b). Moreover, the j_{CO} could be further elevated to nearly 1 A cm^{-2} at –0.7 V *vs*. RHE with an FE of 90.7% and an EE of ~63% (Figure 5b), providing the opportunity to promote CO production by simply applying more negative cathodic potentials while maintaining high selectivity.

Notably, the optimal CO productivity and selectivity could be achieved at a relatively low CO_2 feed flow of 60 sccm (Figure 5c, d). Increasing the flow rate from 20 to 60 sccm could significantly enhance the CO_2RR reactivity, while elevating the flow rate to 80 sccm showed no further noticeable enhancement in FE or effective current density for CO. As shown in Figure 5e, although FE_{CO} values were similar in the flow cell and the H-cell, the production rate for CO was significantly boosted in the flow cell. That is, facilitating the mass transfer of CO_2 with the GDE and flow-cell configuration could significantly promote the CO_2RR activity of H-AuMPs. As a result, the H-AuMPs represented one of the most efficient CO_2RR electrocatalysts, surpassing previously reported ones with high activity, high selectivity, low overpotential, and thus high cathodic energy efficiency (Table S7). Especially, a similar promoting strategy can also be applied to the electrocatalytic dinitrogen reduction reactions for ammonia synthesis, and related work is still in progress in our laboratory.

4 Conclusions

In conclusion, we present a hydrogen peroxide mediated solution synthesis of free-standing and stable multi-twinned gold nanoparticles with tensile lattices and surface steps. Electrochemical, spectroscopic, and computational studies revealed that the tensile Au surface steps exhibited modified electronic structures with strengthened CO_2 adsorption and promoted CO_2 electroreduction reactivity. As a result, the multi-twinned gold nanoparticles with tensile surface steps showed significantly promoted activity and selectivity towards electrocatalytic CO_2 reduction at low overpotentials in aqueous solutions under ambient conditions. Such advantages were further boosted with the use of gas-diffusion layers and flow cells that facilitated the diffusion of gaseous reactants and products. Therefore, upon optimizing the catalysts and reaction interfaces, we can perform electro-

catalytic CO_2 reduction with low overpotential, high selectivity, high activity, and high energy efficiency, and explore their practical applications. A similar strategy may find more applicability in future electrocatalysis.

Acknowledgements We thank the Analytical and Testing Center of BIT for technical support. We acknowledge the financial support from the National Natural Science Foundation of China (21971012, 21922502, and 21971017), the National Key Research and Development Program of China (2020YFB1506300), the Beijing Municipal Natural Science Foundation (JQ20007), and the Beijing Institute of Technology Research Fund Program.

Conflict of interest The authors declare no conflict of interest.

Supporting information The supporting information is available online at http://chem.scichina.com and http://link.springer.com/journal/11426. The supporting materials are published as submitted, without typesetting or editing. The responsibility for scientific accuracy and content remains entirely with the authors.

1 Gao D, Zhou H, Wang J, Miao S, Yang F, Wang G, Wang J, Bao X. *J Am Chem Soc*, 2015, 137: 4288–4291
2 Liu S, Tao H, Zeng L, Liu Q, Xu Z, Liu Q, Luo JL. *J Am Chem Soc*, 2017, 139: 2160–2163
3 Gu J, Hsu CS, Bai L, Chen HM, Hu X. *Science*, 2019, 364: 1091–1094
4 Asadi M, Kim K, Liu C, Addepalli AV, Abbasi P, Yasaei P, Phillips P, Behranginia A, Cerrato JM, Haasch R, Zapol P, Kumar B, Klie RF, Abiade J, Curtiss LA, Salehi-Khojin A. *Science*, 2016, 353: 467–470
5 Jiang K, Siahrostami S, Akey AJ, Li Y, Lu Z, Lattimer J, Hu Y, Stokes C, Gangishetty M, Chen G, Zhou Y, Hill W, Cai WB, Bell D, Chan K, Nørskov JK, Cui Y, Wang H. *Chem*, 2017, 3: 950–960
6 Ross MB, De Luna P, Li Y, Dinh CT, Kim D, Yang P, Sargent EH. *Nat Catal*, 2019, 2: 648–658
7 Goyal A, Marcandalli G, Mints VA, Koper MTM. *J Am Chem Soc*, 2020, 142: 4154–4161
8 Sun K, Cheng T, Wu L, Hu Y, Zhou J, Maclennan A, Jiang Z, Gao Y, Goddard Iii WA, Wang Z. *J Am Chem Soc*, 2017, 139: 15608–15611
9 Kim D, Resasco J, Yu Y, Asiri AM, Yang P. *Nat Commun*, 2014, 5: 4948
10 Fang Y, Flake JC. *J Am Chem Soc*, 2017, 139: 3399–3405
11 Trindell JA, Clausmeyer J, Crooks RM. *J Am Chem Soc*, 2017, 139: 16161–16167
12 Chen Y, Li CW, Kanan MW. *J Am Chem Soc*, 2012, 134: 19969–19972
13 Zhu W, Michalsky R, Metin Ö, Lv H, Guo S, Wright CJ, Sun X, Peterson AA, Sun S. *J Am Chem Soc*, 2013, 135: 16833–16836
14 Zhu W, Zhang YJ, Zhang H, Lv H, Li Q, Michalsky R, Peterson AA, Sun S. *J Am Chem Soc*, 2014, 136: 16132–16135
15 Feng X, Jiang K, Fan S, Kanan MW. *J Am Chem Soc*, 2015, 137: 4606–4609
16 Liu M, Pang Y, Zhang B, De Luna P, Voznyy O, Xu J, Zheng X, Dinh CT, Fan F, Cao C, de Arquer FPG, Safaei TS, Mepham A, Klinkova A, Kumacheva E, Filleter T, Sinton D, Kelley SO, Sargent EH. *Nature*, 2016, 537: 382–386
17 Liu Q, Yang X, Li L, Miao S, Li Y, Li Y, Wang X, Huang Y, Zhang T. *Nat Commun*, 2017, 8: 1407
18 Mariano RG, McKelvey K, White HS, Kanan MW. *Science*, 2017, 358: 1187–1192
19 Li J, Chen G, Zhu Y, Liang Z, Pei A, Wu CL, Wang H, Lee HR, Liu K, Chu S, Cui Y. *Nat Catal*, 2018, 1: 592–600
20 Liu M, Liu M, Wang X, Kozlov SM, Cao Z, De Luna P, Li H, Qiu X, Liu K, Hu J, Jia C, Wang P, Zhou H, He J, Zhong M, Lan X, Zhou Y, Wang Z, Li J, Seifitokaldani A, Dinh CT, Liang H, Zou C, Zhang D, Yang Y, Chan TS, Han Y, Cavallo L, Sham TK, Hwang BJ, Sargent EH. *Joule*, 2019, 3: 1703–1718
21 Yuan X, Zhang L, Li L, Dong H, Chen S, Zhu W, Hu C, Deng W, Zhao ZJ, Gong J. *J Am Chem Soc*, 2019, 141: 4791–4794
22 Cao Z, Kim D, Hong D, Yu Y, Xu J, Lin S, Wen X, Nichols EM, Jeong K, Reimer JA, Yang P, Chang CJ. *J Am Chem Soc*, 2016, 138: 8120–8125
23 Gao D, Zhang Y, Zhou Z, Cai F, Zhao X, Huang W, Li Y, Zhu J, Liu P, Yang F, Wang G, Bao X. *J Am Chem Soc*, 2017, 139: 5652–5655
24 Tang C, Shi J, Bai X, Hu A, Xuan N, Yue Y, Ye T, Liu B, Li P, Zhuang P, Shen J, Liu Y, Sun Z. *ACS Catal*, 2020, 10: 2026–2032
25 Cheng H, Yang N, Liu G, Ge Y, Huang J, Yun Q, Du Y, Sun CJ, Chen B, Liu J, Zhang H. *Adv Mater*, 2020, 32: 1902964
26 Li Z, Fu JY, Feng Y, Dong CK, Liu H, Du XW. *Nat Catal*, 2019, 2: 1107–1114
27 Wang H, Xu S, Tsai C, Li Y, Liu C, Zhao J, Liu Y, Yuan H, Abild-Pedersen F, Prinz FB, Nørskov JK, Cui Y. *Science*, 2016, 354: 1031–1036
28 Xia Y, Xiong Y, Lim B, Skrabalak SE. *Angew Chem Int Ed*, 2009, 48: 60–103
29 Ma Y, Zeng J, Li W, McKiernan M, Xie Z, Xia Y. *Adv Mater*, 2010, 22: 1930–1934
30 Walsh MJ, Yoshida K, Kuwabara A, Pay ML, Gai PL, Boyes ED. *Nano Lett*, 2012, 12: 2027–2031
31 Nørskov JK, Bligaard T, Rossmeisl J, Christensen CH. *Nat Chem*, 2009, 1: 37–46
32 Huang H, Jia H, Liu Z, Gao P, Zhao J, Luo Z, Yang J, Zeng J. *Angew Chem Int Ed*, 2017, 56: 3594–3598
33 Luo M, Zhao Z, Zhang Y, Sun Y, Xing Y, Lv F, Yang Y, Zhang X, Hwang S, Qin Y, Ma JY, Lin F, Su D, Lu G, Guo S. *Nature*, 2019, 574: 81–85
34 Ross MB, Dinh CT, Li Y, Kim D, De Luna P, Sargent EH, Yang P. *J Am Chem Soc*, 2017, 139: 9359–9363
35 Shi C, Hansen HA, Lausche AC, Nørskov JK. *Phys Chem Chem Phys*, 2014, 16: 4720–4727
36 Seh ZW, Kibsgaard J, Dickens CF, Chorkendorff I, Nørskov JK, Jaramillo TF. *Science*, 2017, 355: eaad4998
37 Yang HB, Hung SF, Liu S, Yuan K, Miao S, Zhang L, Huang X, Wang HY, Cai W, Chen R, Gao J, Yang X, Chen W, Huang Y, Chen HM, Li CM, Zhang T, Liu B. *Nat Energy*, 2018, 3: 140–147
38 Kresse G, Furthmüller J. *Phys Rev B*, 1996, 54: 11169–11186
39 Perdew JP, Burke K, Ernzerhof M. *Phys Rev Lett*, 1996, 77: 3865–3868
40 Hammer B, Hansen LB, Nørskov JK. *Phys Rev B*, 1999, 59: 7413–7421
41 Grimme S. *J Comput Chem*, 2006, 27: 1787–1799
42 Peterson AA, Abild-Pedersen F, Studt F, Rossmeisl J, Nørskov JK. *Energy Environ Sci*, 2010, 3: 1311–1315
43 Wang M, Shi H, Tian M, Chen R, Shu J, Zhang Q, Wang Y, Li C, Wan N, Lei S. *ACS Appl Nano Mater*, 2021, 4: 11017–11030
44 Wang M, Song R, Zhang Q, Li C, Xu Z, Liu G, Wan N, Lei S. *Fuel*, 2022, 321: 124101
45 Monzó J, Malewski Y, Kortlever R, Vidal-Iglesias FJ, Solla-Gullón J, Koper MTM, Rodriguez P. *J Mater Chem A*, 2015, 3: 23690–23698
46 Adit Maark T, Nanda BRK. *J Phys Chem C*, 2017, 121: 4496–4504
47 Jansonius RP, Reid LM, Virca CN, Berlinguette CP. *ACS Energy Lett*, 2019, 4: 980–986
48 Dinh CT, Burdyny T, Kibria MG, Seifitokaldani A, Gabardo CM, García de Arquer FP, Kiani A, Edwards JP, De Luna P, Bushuyev OS, Zou C, Quintero-Bermudez R, Pang Y, Sinton D, Sargent EH. *Science*, 2018, 360: 783–787
49 Luo M, Wang Z, Li YC, Li J, Li F, Lum Y, Nam DH, Chen B, Wicks J, Xu A, Zhuang T, Leow WR, Wang X, Dinh CT, Wang Y, Wang Y, Sinton D, Sargent EH. *Nat Commun*, 2019, 10: 5814
50 García de Arquer FP, Dinh CT, Ozden A, Wicks J, McCallum C, Kirmani AR, Nam DH, Gabardo C, Seifitokaldani A, Wang X, Li YC, Li F, Edwards J, Richter LJ, Thorpe SJ, Sinton D, Sargent EH. *Science*, 2020, 367: 661–666